

Reversible engineering the spin-orbit coupling of monolayer MoS₂ via laser irradiation under controlled gas atmospheres

Xilong Liang,^{1,2} Chengbing Qin,^{1,2*} Yan Gao,^{1,2,3} Shuangping Han,^{1,2} Guofeng Zhang,^{1,2} Ruiyun Chen,^{1,2} Jianyong Hu,^{1,2} Liantuan Xiao,^{1,2*} and Suotang Jia^{1,2}

¹ State Key Laboratory of Quantum Optics and Quantum Optics Devices, Institute of Laser Spectroscopy, Shanxi University, Taiyuan, Shanxi 030006, China.

² Collaborative Innovation Center of Extreme Optics, Shanxi University, Taiyuan, Shanxi 030006, China.

³ Department of Physics, Shanxi Datong University, Datong, 037009, China.

* Author to whom correspondence should be addressed.

E-mail:

Chengbing Qin, chbqin@sxu.edu.cn

Liantuan Xiao, xlt@sxu.edu.cn

Abstract

Monolayer transition metal dichalcogenides (TMDs) with strong spin-orbit coupling (SOC) combined with broken inversion symmetry, leading to a coupling of spin and valley degrees of freedom. These unique features make TMDs highly interesting for potential spintronics and valleytronic applications. However, engineering SOC at room temperature as demand after device fabrication is still a great challenge for their practical applications. Here we reversibly engineer the spin-orbit coupling of monolayer MoS₂ by laser irradiation under controlled gas environments, where the spin-orbit coupling has been effectively regulated within 120 meV to 200 meV. Furthermore, the photoluminescence (PL) intensity of B exciton can be invertible manipulation over 2 orders of magnitude. We attribute the engineering of spin-orbit coupling to the reduction of binding energy combined with band renormalization, originating from the enhanced absorption coefficient of monolayer MoS₂ under inert gases and subsequent the significantly boosted carrier concentrations. Reflectance contrast spectra during the engineering stage provide unambiguous proof to support our interpretation. Our approach offers a new avenue to actively control the SOC strength in TMDs materials at room temperature and paves the way for designing innovative spintronics devices.

1. Introduction

Spin-orbit coupling (SOC), the relativistic interaction between the spin and momentum degrees of freedom of electrons^[1], has attracted tremendous attention both for their interesting fundamental physics and potential applications in next-generation devices^[2-4]. Essentially, SOC plays a crucial role in condensed-matter physics and accounts for a broad range of fascinating phenomena, such as spin Hall effects^[5,6], topological insulation^[7,8], Majorana and Weyl fermion^[9,10]. On the other side, this interaction also provides a route towards manipulation of electron spins and thus lies at the core of spintronics^[11,12]. According to the symmetry dependence, two alternative mechanisms are responsible for the origin of spin-orbit coupling. For the symmetry-independent case, SOC originates from the spin-orbit interaction in atomic orbitals and thus exists in almost all the physics systems^[13]. Nonetheless, the symmetry-dependent SOC is only present in crystal structures with broken inversion symmetry, which can be further subdivided into two different types, namely Dresselhaus and Rashba SOC, related to different sources of the electric field asymmetry^[14]. Dresselhaus effect is caused by the bulk-induced asymmetry (surviving in the materials without any inversion centers), while the Rashba term is originating from surface- or interface-induced asymmetry (occurring in the systems with broken out-of-plane mirror symmetry)^[15]. Generally, these two types of SOC naturally coexist and act on the electron spin as an effective magnetic field^[16]. Despite the encouraging progress on the generation and manipulation of SOC in many physical systems (including ultra-cold atoms^[17], quantum wells^[18], nanowires^[19], and organic semiconductors^[6]), however,

exploring the practical spintronic devices at room temperatures still has proven difficult due to their modest spin-orbit interaction. To this end, physical systems with enhanced SOC are highly desirable^[20].

Recent development in atomic-layered transition metal dichalcogenides (TMDs) with chemical formula MX_2 (such as MoS_2 , MoSe_2 , WS_2 , and WSe_2) demonstrate that^[21,22], TMDs are expected to be good candidates for spintronic technologies at room temperatures, due to their giant intrinsic SOC^[20,23]. The spin-orbit splittings (characterizing the strength of SOC) in TMDs monolayer induced by spin-orbit interaction are several hundred millielectron volts (meV) at the top of the valence band and a few to tens of meV for the bottom conduction band^[22,24]. The origin of this dramatic interaction lies in the relative heavy elements in the TMDs materials and the involvement of the transition metal d orbitals^[25]. Specifically, the valence band at the K point of the Brillouin zone is primarily composed of the $d_{x^2-y^2}$ and d_{xy} orbitals of the metal atom^[20,26]. This giant splitting defines two different excitons attached to the two spin-split valence subbands, namely A and B excitons, respectively. On the other hand, the conduction band predominantly arises from the d_{z^2} orbital of the metal atom, and thus no significant splitting is expected. Nonetheless, a small spin splitting is still survived after considering the role of less strongly coupled chalcogenide orbitals and the higher-order effect of the metal orbital^[27-29]. Despite the giant splitting in the valence bands, engineering spin-orbit splitting is still strongly desired, which is an indispensable element of spintronics. Theoretical calculations have predicted that the spin-orbit splitting in TMDs monolayer can be effectively controlled via charge

doping^[30], biaxial strain^[31,32], as well as co-doping of fluorine and group VA elements^[33]. Very recently, spin-orbit engineering in $\text{Mo}_{(1-x)}\text{W}_x\text{Se}_2$ alloy monolayers have been experimentally demonstrated, in the view of the critical role of the transition metal d orbitals^[34].

Here, we experimentally demonstrated the engineering of the spin-orbit splitting of monolayer MoS_2 through laser irradiation under gas-controlled environments. We show that the spin-orbit splitting, *i.e.*, the splitting between A and B excitons, can be enlarged from 152 meV of the as-prepared sample to 200 meV after irradiation with 532 nm continuum-wave (CW) laser under inert gas atmospheres (including N_2 and He). The photoluminescence (PL) intensity of B exciton has also been enhanced by more than two orders of magnitude in this stage. We further proved that the enhanced splitting could be reversibly reduced to 120 meV through laser irradiation under air or O_2 atmosphere, associated with the recovery of PL intensity of B exciton. We attribute the reversible engineering of spin-orbit splitting and PL modulation to the enhanced absorption coefficient of monolayer MoS_2 and subsequent the increase of carriers concentrations, resulting in the significant Auger recombination and pronounced band renormalization. This hypothesis has been confirmed by the reflectance contrast spectra during the engineering of spin-orbit interaction. Our approach provides new opportunities for reversible manipulating SOC in monolayer TMDs after device fabrications at the desired locations, which has important implications in designing future spintronics devices.

2. Results and Discussion

For this study, monolayer MoS₂ was prepared by traditional chemical vapor deposition (CVD) on the Si/SiO₂ substrate (Six Carbon Technology Shenzhen)^[35]. Fig. 1a presents the optical image of a typical sample. Isolated single-crystal MoS₂ flakes with a triangular shape and edge lengths ranging from 10 to 30 μm can be visualized. We verify the thickness of these flakes to be monolayer by atomic force microscopy (AFM), as presented in Fig. S1. Almost uniform PL intensity (Fig. 1b) further confirms the high quality of the prepared sample. The corresponding PL spectra have been conducted with the excitation of 532 nm continuum-wave (CW) laser (as the arrow shown in Fig. 1c). The spectral profile can be deconvoluted into two components, with the energy of 1.824 eV and 1.976 eV, respectively. Straightforward, the two peaks can be attributed to the A and B excitons of monolayer MoS₂, with the spin-orbit splitting of 152 meV. The energy of excitons, the spin-orbit splitting, and the PL intensity ratio between A and B excitons are well consistent with the relevant reports^[36-38].

The optical experiments, including laser irradiation, PL spectra measurements, as well as micropatterning, were performed by using a home-built scanning confocal microscope. The schematic diagram can be found in our previous works and electronic supplementary materials (Fig. S2)^[39,40]. Specifically, the prepared sample was placed on a motorized three-dimensional piezoelectric ceramics nano stage, which was covered by a polymethyl methacrylate (PMMA) chamber with a control vacuum valve on top of the plane. MoS₂ was engineered by a 532 nm CW laser via an objective (Nikon, 100×, NA 0.9), where PL was also collected by the same objective. All the experiments

can be mainly divided into two cases. One is engineering monolayer MoS₂ with blowing N₂ gases (labeled as N₂), the other is irradiating the sample blowing the dry air gases (labeled as air).

Figure 1d presents a typical PL trajectory of monolayer MoS₂ under laser irradiation against gas cycling. The irradiation and excitation of the MoS₂ sample are both performed by the 532 nm CW laser with a power density of 21 MW/cm². For the pristine sample in air condition, PL is slightly enhanced (roughly twice) under laser irradiation (Fig. S5), which has been reported by our previous work and other groups^[39,41,42]. This phenomenon can be understood as the formation of defects and adsorption of O₂/H₂O gas molecules, which will result in the depletion of free electrons and the conversion from A^T to A⁰. Further irradiation in air condition will lead to the damage of crystal and the quenching of PL (Fig. S5). However, further irradiation in N₂ atmosphere emerges an entirely new phenomenon, where PL can be significantly enhanced by orders of magnitude (from 16 kcps (thousand counts/s) to 457 kcps) and can maintain the maximum PL without any quenching, as presented in Fig. 1d. Intriguingly, this enhanced PL can be inverted to the initial value in the air atmosphere by switching N₂ to air gases. In this case, PL will reduce rapidly and tend to a stable value almost in one minute. Even more intriguingly, this enhancement and reversal can be manipulated circularly merely by switching the N₂ and air atmosphere, as presented in Fig. 1d.

To reveal the underlying mechanism, PL trajectory of the first circle is divided into four stages, highlighted by different colors, as shown in Fig. 2a. To explore the

reversible proceeding (PL quenching in air atmosphere) more clearly, here we used a relatively low power density (3.5 MW/cm^2) to slow down the quenching process. PL spectra of the four stages have been conducted, as presented in Fig. 3b to 3e, respectively. All the spectral profiles can be well deconvoluted into A and B excitons by Voigt functions (typical fitting curves can be found in Fig. S4). The determined photon energies, full width at half maximum (FWHM), integrated intensities, and the corresponding spectral weights for A and B excitons have been presented in Fig. 3f to 3i, respectively (see Fig. S5 for detailed comparison). Now we provide a comprehensive description of the four stages.

- (I) In stage I, PL of A exciton is undoubtedly enhanced, which can be attributed to the conversion from A^T to A^0 , as we discussed above and reported in the previous works^[39,41,42]. We also find that the photon energy of B exciton emerges slightly redshift, which possibly originates from the formation of new defects and the reconstruction of the band structure.
- (II) In stage II, the FWHM of B exciton dramatically increases from 90 meV to 336 meV. That's to say, the same amount of B exciton has been distributed into a broad energy region when blowing N_2 . This unusual broadening of FWHM will not further increase with prolonged irradiation times, as shown in stage III. On the other hand, the integrated PL abruptly quenched. From Fig. 2h, we can find that PL intensity of A exciton almost quenches to the background, while that of B exciton presents slight enhancement. The conversion between A and B excitons can also

be observed from the variation of their spectral weight (the ratio of the integrated PL intensity of each component to the total intensity), as shown in Fig. 2i. One should emphasize that both stage I and II cannot be restored by switching N₂ to air again. We have confirmed that these two stages can be entirely removed by blowing N₂ to the pristine sample with several minutes, rather than by experimenting within the air atmosphere as a starting point (Fig. 5).

(III) In stage III, we can find PL intensity of B exciton incredibly enhanced from 242 kcps for the pristine sample to the maximum 25191 kcps, corresponding to more than two orders of magnitude enhancement. Another distinguishing characteristic is that FWHM of B exciton has remained around 320 meV (Fig. 2g), much broader than the initial value. Thus, PL spectra feature an extremely broadband. During this stage, PL of A exciton is also enlarged by 3 times, with a remarkable redshift in its photon energy and broadening in its FWHM.

(IV) After removing N₂, photon energies, FWHM, and PL intensities of both A and B excitons will be restored to the beginning of stage III. The abrupt change of photon energy and FWHM between stages III and IV are probably due to the excitation power switching from 21 MW/cm² to 3.5 MW/cm². Further switching the air to N₂, PL intensity, as well as the corresponding parameters, can be reversibly engineered, as presented in Fig. 1d.

Beyond the variation of PL intensity and FWHM, photon energy of the two excitons also show dramatic changes. During stage III and IV, A exciton presents

successive redshift from 1.826 eV to 1.785 eV (stage III), and then reverts back to 1.825 eV (stage IV). On the other aspect, B exciton shows more complex behavior. Its photon energy shifts from 1.963 eV to 1.996 eV at the initial of stage III, and then constantly softens to 1.979 eV. In stage IV, photon energy of B exciton restores to 1.944 eV, as presented in Fig. 2f. The spin-orbit splitting can be determined by subtracting the photon energy of B from that of A, as shown in Fig. 3. We can find that the splitting increases from 140 meV (at the initial of stage III) to 200 meV (at the end of stage IV), and then recovers to close 140 meV at the end of stage IV. As we expected the spin-orbit splitting during stages III and IV can be invertible engineered when we recurrently switch N₂ and air atmosphere. However, the splitting during stages I and II cannot be restored, as we discussed above. This phenomenon indicates that we can reversibly manipulate the spin-orbit coupling of monolayer MoS₂ as demand by laser irradiation, with the switching of N₂ and air gases.

To optimize engineering and demonstrate the robustness of this approach, we further perform a systematic study. Firstly, we prove that oxygen (O₂) plays a vital role in the PL quenching process by changing the air to the pure O₂, as shown in Fig. 4a. Note that PL quenches to the minimum value in hundreds of seconds (under 17.5 MW/cm²) when blowing pure air gases. Yet, this process is almost one order of magnitude faster when blowing pure O₂ gas. This can be understood as the density of O₂ in the pure oxygen atmosphere is five times of that in the air atmosphere (the two most dominant components in air are 21% O₂ and 78% N₂). We farther verify that the reversible engineering of the spin-orbit splitting of monolayer MoS₂ and the

corresponding PL enhancement can be achieved in other inert gases, such as helium (He) in Fig. 4b. PL evolution in He is similar to that in N₂ as well, as presented in Fig. S6. It is worth mentioning that both PL enhancing and quenching in He condition are faster than that in N₂ atmosphere. To exclude the thermal effect from the CW laser irradiation with high power density, we switch off the laser during the enhancing process in N₂ atmosphere, as presented in Fig. 4c. Note that when we switch off the laser for several minutes (even several hours) and hold the N₂ atmosphere, the enhanced PL intensity still maintains when we switch on the laser again. If we switch off the laser and stop the N₂ blowing, PL emerges a slight quenching and then shows the subsequent enhancement when the N₂ blowing is restored. This slight quenching originates from the resident air when the laser is switched on. This result hints that the spin-orbit coupling engineering through our approach is robust and reliable. The modified splitting persists even without laser irradiation and blowing N₂ atmosphere (Fig. 4c), manifesting great potential applications of monolayer MoS₂ in diverse spintronic and Valleytronic devices.

The power-dependent PL evolutions are also performed to optimize the engineering process. As illustrated in Fig. 4d and 4e, PL enhancement in N₂ atmosphere and the subsequent PL quenching in air condition at the laser power density ranging from 3.5 MW/cm² to 17.5 MW/cm² have been determined in our experiment. For both processes, the higher the power density, the faster the enhancing and quenching rate. We find that PL enhancement can be empirically fitted by the formula, $I(t) = I_s + (I_0 - I_s) \cdot \left\{ 1 + \exp\left[(t - t_0) \cdot \gamma_{\uparrow}\right] \right\}^{-1}$, where I_s and I_0 denote the saturation and

initial PL intensity, and γ_{\uparrow} is the rate of the enhancement process. The fit results, as the solid lines shown in Fig. 4d, are in good agreement with experimental data. The determined γ_{\uparrow} as a function of power density is presented in Fig. S7, from which the acceleration of the enhancement process with the increase of power density can be determined. On the contrary, PL quenching processes can be well fitted by a bi-exponential function $I(t) = I_0 + A_1 \cdot e^{-t\gamma_1} + A_2 \cdot e^{-t\gamma_2}$ (as the solid lines presented in Fig. 4e). Fascinatingly, the averaged rate of the quenching process, $\gamma_{\downarrow} = (A_1\gamma_1 + A_2\gamma_2) / (A_1 + A_2)$, falls exponentially with the increase of laser power, as illustrated in Fig. S7. Although the mechanisms behind the two empirical equations are under debate and further works are needed, these parameters still can provide a guideline to precisely control the spin-orbit coupling and PL intensity of monolayer MoS₂.

Now we can declare that the observed optical behaviors of monolayer MoS₂ are profoundly different from the phenomena reported in the previous works, where PL enhancing and quenching were mostly attributed to the conversion between A^T and A⁰[41,42], due to the formation of new defects and the depletion of free electrons[43,44]. However, the maintained maximum PL intensity and reversible features indicate that laser irradiation does not cause further damage to the crystal structure in N₂ or He atmosphere, rather than that in air condition[41,42]. To explore the reversible engineering of the spin-orbit coupling and the corresponding PL intensity, we propose a plausible scenario, as presented in Fig. 5. As we discussed above, the valence band (VB) will split into two subbands (A and B) due to the spin-orbital coupling. After laser excitation, electrons will populate at the lowest conduction band (CB), while holes occupy the

highest valence band, resulting in the strong emission of A exciton via radiative recombination, as shown in Fig. 5a. Generally, the radiative and non-radiative processes of excitons in monolayer MoS₂ can be expressed as $G=An+Bn^2+Cn^3$, where G is the carrier generation/recombination rate^[45]. n is the photo-excited carrier (electron/hole) concentrations. A, B, and C represent the non-radiative Shockley-Read-Hall, radiative recombination, and Auger recombination coefficients, respectively. Here Auger recombination represents the annihilation of an exciton (an electron in the conduction band and a hole in A subband) and an electron in B subband, as shown in Fig. 5b. This phonon-assisted Auger recombination will result in the formation of holes in B subband (Fig. 5c). The radiative recombination between the electrons in the conduction band and the holes in B subband brings PL emission of B exciton (Fig. 5d). From the equation, we can find that Auger recombination becomes dominant at high carrier concentrations. In other words, the higher the carrier concentrations, the stronger the emission of B exciton. In our experiment, the excitation power density was maintained for each measurement, which is not responsible for the increase of carrier concentrations. Potential contributions from laser-induced thermal effect have also been excluded by the PL evolution between switching on and off the laser irradiation (Fig. 4c).

Ultimately, we tentatively attribute the increase of carrier concentrations to the enhanced absorption coefficient of monolayer MoS₂ under the blowing of inert gases (N₂ and He). The enhanced coefficient probably results from the replacement of adsorbed O₂ by inert gases, where laser irradiation provides the activated energy to overcome the barrier of the replacement reactions. Considering that the quenching

processes are much faster than the enhancing processes under laser irradiation with the same power density, we can speculate that the activated energy of the forward reaction (replacing O₂ by inert gases) is higher than that of the backward reaction (replacing inert gases by O₂). The elevated carrier densities not only enhance the Auger recombination but also result in screened Coulomb interaction between charge carriers and possible dense electron-hole plasma^[46,47]. According to the previous works,^[25,48-50] this produces a pronounced many-particle renormalization effect, broaden the linewidth of resonant excitons, as well as reduce both the optical gap and exciton binding energies. The linewidth broadening is in agreement with our results, as shown in Fig. 2g. For the A exciton (X^A), the reduction of the optical gap is more pronounced. Hence the optical transition of A exciton is redshift, as we determined in Fig. 2f. Nevertheless, for the B exciton (X^B), we speculate that the reduction of binding energy is more significant (as shown in Fig. 5c), resulting in the blueshift of its photon energy. Consequently, the spin-orbit splitting in the conduction band (Δ_{SO}^{CB}) has been enlarged from a few meV to tens of meV. And more importantly, it can be reversibly engineering as demand by an all-optical procedure without any external electric field.

To prove our hypothesis, we further perform the reflectance contrast spectra during stage III and IV, respectively, as shown in Fig. 5e and 5f. Here $\Delta R/R=(R_{MoS_2}-R_{Si/SiO_2})/R_{Si/SiO_2}$, where R_{MoS_2} and R_{Si/SiO_2} are the reflected light intensity (see methods). At the beginning of stage III, two peaks around 1.88 eV and 2.01 eV can be determined in the reflectance contrast spectra, coinciding with the absorption of A and B excitons reported in the relevant works^[36]. With the increase of laser irradiation in N₂ atmosphere,

the enhancement and broadening of reflectance spectra can be demonstrated, indicating the validity of our hypothesis. The full recovery of the reflectance contrast spectra in stage IV (Fig. 5f) further supports our conclusions.

Although a plausible mechanism has been proposed, further experiments are still needed to clarify the crucial roles of O₂ and inert gases, as well as Auger recombination. Firstly, comprehensive calculations, taking carriers density and Auger recombination into account, should be performed to reveal the role of inert gases and O₂ in the photoexcited carriers as well as the spin-orbit splitting associating with the variation of carriers density. Secondly, crystal inversion symmetry breaking together with strong SOC leads to coupled spin and valley in TMDs monolayer.^[51] Reversible engineering of SOC offers opportunities for controls of spin and valley in these materials, providing a new route to design the high-performance monolayer TMDs-based valleytronics and opto-valleytronics. Furthermore, this coupling results in an energy separation between the spin-allowed and optically active transitions, as well as the spin-forbidden and optically inactive transitions, namely bright and dark excitons.^[52-54] The engineering of SOC changes the carrier populations between the two transitions, and thus new evidences and novel physics may be determined by further experiments. At last but not end, the kinetics of the replacement reaction typically depends upon temperature and the concentration of reactants. Thus, the enhancing and quenching processes may be controlled by changing the temperature of monolayer MoS₂, as well as the concentrations of O₂, N₂, or He. Particularly, the temperature-dependent PL spectra manifest abundant information involving the increase of FWHM and the exciton-

phonon scattering (Auger recombination).

3. Conclusion

In conclusion, we have reversibly engineered spin-orbit splitting and PL emission of B exciton in monolayer MoS₂ by laser irradiation under controlled gas environments (switching between inert gases, such as N₂ and He, and air atmosphere). PL spectra evolutions during the reversible manipulation and power-dependent PL behaviors have been conducted and analyzed. The spin-orbit splitting is modified between 120 meV and 200 meV. PL intensity of B exciton has been enhanced by two orders of magnitude. We also show that the reversible and controllable PL spectral features enable explorations of versatile optical applications, such as optical recording ([Fig. S8](#)). After excluding the thermal effect originating from the CW laser irradiation with high power, we propose a plausible mechanism to explore this unique PL feature, where the emission of B exciton is attributed to the photon-assisted Auger recombination. We suggest that Auger recombination can be modified during the replacement reactions between inert and air gases. However, the underlying physics remains elusive and needs to study further.

Acknowledgement

The authors gratefully acknowledge support from the National Key Research and Development Program of China (Grant No. 2017YFA0304203), Natural Science Foundation of China (Nos. 91950109, 61875109, 61527824, and 61675119), Natural Science Foundation of Shanxi Province (No. 201901D111010(ZD)), PCSIRT (No. IRT_17R70), 111 project (Grant No. D18001), 1331KSC, and PTIT.

Method

Optical measurements. Schematic of the experimental setup is presented in Fig. S2. A home-built scanning confocal system based on an invert microscope (Nikon, TE2000-U) was used to engineer monolayer MoS₂ and take PL spectroscopy, by utilizing a 532 nm CW laser (MSL-III-532, Changchun New Industries Optoelectronics Tech. Co., Ltd.). After extended by a beam expander and filtered by an excitation filter (LL01-532-25, Semrock), the laser was directed by a dichroic mirror (Di01-RE532, Semrock) towards a dry objective (100×, NA 0.9, Nikon) to engineer and excite the monolayer MoS₂, which was placed on a motorized three-dimensional piezoelectric ceramics nano stage (200/20SG, Tritor). The laser spot diameter was around 1 μm. PL from MoS₂ was collected by the same objective and passed through the dichroic mirror and a notch filter (NF03-532E-25, Semrock). Then, PL was split into two beam by a beam splitter with the ratio of 7 to 3. The weaker one was further filtered spatially by a 100 μm spatial filter and an emission filter (LP03-532RE-25, Semrock) to block the back scattered

laser light. PL intensity was detected by a single photon detector (SPCM-AQR-15, PerkinElmer). The stronger beam was sent through a monochromator with the focal length of 30 cm, equipped with a charge-coupled device (DR-316B-LDC, Andor). Monolayer MoS₂ was covered by a polymethyl methacrylate (PMMA) chamber with a control vacuum valve on top of the plane (Fig. S3). Dry air, N₂, He, and O₂ with controlled flow rate were used to blow the sample. All the experiments was performed at room temperature. For the reflectance contrast measurements, a broadband light (DH-2000-BAL, Ocean Optics) was focused onto the sample by the same objective.

References

- (1). Soumyanarayanan, A.; Reyren, N.; Fert, A., *et al.*, Emergent phenomena induced by spin-orbit coupling at surfaces and interfaces. *Nature* **2016**, *539*, 509-517.
- (2). Smidman, M.; Salamon, M. B.; Yuan, H. Q., *et al.*, Superconductivity and spin-orbit coupling in non-centrosymmetric materials: a review. *Rep Prog Phys* **2017**, *80*, 036501.
- (3). Manchon, A.; Koo, H. C.; Nitta, J., *et al.*, New perspectives for Rashba spin-orbit coupling. *Nat Mater* **2015**, *14*, 871-82.
- (4). Lin, Y. J.; Jimenez-Garcia, K.; Spielman, I. B., Spin-orbit-coupled Bose-Einstein condensates. *Nature* **2011**, *471*, 83-6.
- (5). Kato, Y. K.; Myers, R. C.; Gossard, A. C., *et al.*, Observation of the spin hall effect in semiconductors. *Science* **2004**, *306*, 1910-1913.
- (6). Sun, D.; van Schooten, K. J.; Kavand, M., *et al.*, Inverse spin Hall effect from pulsed spin current in organic semiconductors with tunable spin-orbit coupling. *Nat Mater* **2016**, *15*, 863-9.
- (7). Hasan, M. Z.; Kane, C. L., Colloquium: Topological insulators. *Rev Mod Phys* **2010**, *82*, 3045-3067.
- (8). Fan, Y.; Upadhyaya, P.; Kou, X., *et al.*, Magnetization switching through giant spin-orbit torque in a magnetically doped topological insulator heterostructure. *Nat Mater* **2014**, *13*, 699-704.
- (9). Desjardins, M. M.; Contamin, L. C.; Delbecq, M. R., *et al.*, Synthetic spin-orbit interaction for Majorana devices. *Nat Mater* **2019**, *18*, 1060-1064.
- (10). Burkov, A. A.; Balents, L., Weyl semimetal in a topological insulator multilayer. *Phys Rev Lett* **2011**, *107*, 127205.
- (11). Baltz, V.; Manchon, A.; Tsoi, M., *et al.*, Antiferromagnetic spintronics. *Rev Mod Phys* **2018**, *90*, 015005.
- (12). Han, W.; Kawakami, R. K.; Gmitra, M., *et al.*, Graphene spintronics. *Nat Nanotechnol* **2014**, *9*, 794-807.
- (13). Premasiri, K.; Radha, S. K.; Sucharitakul, S., *et al.*, Tuning Rashba Spin–Orbit

- Coupling in Gated Multilayer InSe. *Nano Lett* **2018**, *18*, 4403-4408.
- (14). Premasiri, K.; Gao, X. P. A., Tuning spin-orbit coupling in 2D materials for spintronics: a topical review. *J Phys Condens Matter* **2019**, *31*, 193001.
- (15). Nowak, M. P.; Szafran, B.; Peeters, F. M., *et al.*, Tuning of the spin-orbit interaction in a quantum dot by an in-plane magnetic field. *Phys Rev B* **2011**, *83*, 245324.
- (16). Sasaki, A.; Nonaka, S.; Kunihashi, Y., *et al.*, Direct determination of spin-orbit interaction coefficients and realization of the persistent spin helix symmetry. *Nat Nanotechnol* **2014**, *9*, 703-9.
- (17). Huang, L.; Meng, Z.; Wang, P., *et al.*, Experimental realization of two-dimensional synthetic spin-orbit coupling in ultracold Fermi gases. *Nat Phys* **2016**, *12*, 540-544.
- (18). Herranz, G.; Singh, G.; Bergeal, N., *et al.*, Engineering two-dimensional superconductivity and Rashba spin-orbit coupling in LaAlO₃/SrTiO₃ quantum wells by selective orbital occupancy. *Nat Commun* **2015**, *6*, 6028.
- (19). Nadj-Perge, S.; Frolov, S. M.; Bakkers, E. P., *et al.*, Spin-orbit qubit in a semiconductor nanowire. *Nature* **2010**, *468*, 1084-7.
- (20). Zhu, Z. Y.; Cheng, Y. C.; Schwingenschlögl, U., Giant spin-orbit-induced spin splitting in two-dimensional transition-metal dichalcogenide semiconductors. *Phys Rev B* **2011**, *84*, 153402.
- (21). Chhowalla, M.; Shin, H. S.; Eda, G., *et al.*, The chemistry of two-dimensional layered transition metal dichalcogenide nanosheets. *Nat Chem* **2013**, *5*, 263-75.
- (22). Xu, X.; Yao, W.; Xiao, D., *et al.*, Spin and pseudospins in layered transition metal dichalcogenides. *Nat Phys* **2014**, *10*, 343-350.
- (23). Zhou, B. T.; Taguchi, K.; Kawaguchi, Y., *et al.*, Spin-orbit coupling induced valley Hall effects in transition-metal dichalcogenides. *Commun Phys* **2019**, *2*, 26.
- (24). Delhomme, A.; Butseraen, G.; Zheng, B., *et al.*, Magneto-spectroscopy of exciton Rydberg states in a CVD grown WSe₂ monolayer. *Appl Phys Lett* **2019**, *114*, 232104.
- (25). Wang, G.; Chernikov, A.; Glazov, M. M., *et al.*, Colloquium: Excitons in atomically thin transition metal dichalcogenides. *Rev Mod Phys* **2018**, *90*, 021001.
- (26). Braganca, H.; Riche, F.; Qu, F., *et al.*, Dark-exciton valley dynamics in transition

- metal dichalcogenide alloy monolayers. *Sci Rep* **2019**, *9*, 4575.
- (27). Marinov, K.; Avsar, A.; Watanabe, K., *et al.*, Resolving the spin splitting in the conduction band of monolayer MoS₂. *Nat Commun* **2017**, *8*, 1938.
- (28). Kosmider, K.; Gonzalez, J. W.; Fernandez-Rossier, J., Large spin splitting in the conduction band of transition metal dichalcogenide monolayers. *Phys Rev B* **2013**, *88*, 245436.
- (29). Liu, Y.; Tom, K.; Zhang, X., *et al.*, Alloying effect on bright–dark exciton states in ternary monolayer Mo_xW_{1-x}Se₂. *New J Phys* **2017**, *19*, 073018.
- (30). Chen, J.; Wu, K.; Ma, H., *et al.*, Tunable Rashba spin splitting in Janus transition-metal dichalcogenide monolayers via charge doping. *RSC Adv* **2020**, *10*, 6388-6394.
- (31). Absor, M. A. U.; Santoso, I.; Harsojo, *et al.*, Polarity tuning of spin-orbit-induced spin splitting in two-dimensional transition metal dichalcogenides. *J Appl Phys* **2017**, *122*, 153905.
- (32). Absor, M. A. U.; Kotaka, H.; Ishii, F., *et al.*, Strain-controlled spin splitting in the conduction band of monolayer WS₂. *Phys Rev B* **2016**, *94*, 115131.
- (33). Guo, S.; Zheng, H.; Wang, Y., *et al.*, Achieving giant spin-orbit splitting in conduction band of monolayer WS₂ via n-p co-doping. *AIP Adv* **2019**, *9*, 075304.
- (34). Wang, G.; Robert, C.; Suslu, A., *et al.*, Spin-orbit engineering in transition metal dichalcogenide alloy monolayers. *Nat Commun* **2015**, *6*, 10110.
- (35). Zhou, D.; Shu, H.; Hu, C., *et al.*, Unveiling the Growth Mechanism of MoS₂ with Chemical Vapor Deposition: From 2D Planar Nucleation to Self-Seeding Nucleation. *Crystal Growth & Design* **2018**, *18*, 1012-1019.
- (36). Dhakal, K. P.; Duong, D. L.; Lee, J., *et al.*, Confocal absorption spectral imaging of MoS₂: optical transitions depending on the atomic thickness of intrinsic and chemically doped MoS₂. *Nanoscale* **2014**, *6*, 13028-35.
- (37). Kim, J. G.; Yun, W. S.; Jo, S., *et al.*, Effect of interlayer interactions on exciton luminescence in atomic-layered MoS₂ crystals. *Sci Rep* **2016**, *6*, 29813.
- (38). Jung, Y.; Shen, J.; Cha, J. J., Surface effects on electronic transport of 2D chalcogenide thin films and nanostructures. *Nano Converg* **2014**, *1*, 18.
- (39). Qin, C.; Gao, Y.; Zhang, L., *et al.*, Flexible engineering of light emission in

- monolayer MoS₂ via direct laser writing for multimode optical recording. *AIP Adv* **2020**, *10*, 045230.
- (40). Qin, C.; Qiao, Z.; He, W., *et al.*, Laser-driven propulsion of multilayer graphene oxide flakes. *J Mater Chem C* **2018**, *6*, 2329-2335.
- (41). Oh, H. M.; Han, G. H.; Kim, H., *et al.*, Photochemical Reaction in Monolayer MoS₂ via Correlated Photoluminescence, Raman Spectroscopy, and Atomic Force Microscopy. *ACS Nano* **2016**, *10*, 5230-6.
- (42). Ardekani, H.; Younts, R.; Yu, Y., *et al.*, Reversible Photoluminescence Tuning by Defect Passivation via Laser Irradiation on Aged Monolayer MoS₂. *ACS Appl Mater Interfaces* **2019**, *11*, 38240-38246.
- (43). Tongay, S.; Zhou, J.; Ataca, C., *et al.*, Broad-Range Modulation of Light Emission in Two-Dimensional Semiconductors by Molecular Physisorption Gating. *Nano Lett* **2013**, *13*, 2831-2836.
- (44). Mouri, S.; Miyauchi, Y.; Matsuda, K., Tunable Photoluminescence of Monolayer MoS₂ via Chemical Doping. *Nano Lett* **2013**, *13*, 5944-5948.
- (45). Salehzadeh, O.; Tran, N. H.; Liu, X., *et al.*, Exciton kinetics, quantum efficiency, and efficiency droop of monolayer MoS₂ light-emitting devices. *Nano Lett* **2014**, *14*, 4125-30.
- (46). Steinhoff, A.; Kim, J. H.; Jahnke, F., *et al.*, Efficient Excitonic Photoluminescence in Direct and Indirect Band Gap Monolayer MoS₂. *Nano Lett* **2015**, *15*, 6841-7.
- (47). Yu, Y.; Bataller, A. W.; Younts, R., *et al.*, Room-Temperature Electron-Hole Liquid in Monolayer MoS₂. *ACS Nano* **2019**, *13*, 10351-10358.
- (48). Erben, D.; Steinhoff, A.; Gies, C., *et al.*, Excitation-induced transition to indirect band gaps in atomically thin transition-metal dichalcogenide semiconductors. *Phys Rev B* **2018**, *98*, 035434.
- (49). Koperski, M.; Molas, M. R.; Arora, A., *et al.*, Optical properties of atomically thin transition metal dichalcogenides: observations and puzzles. *Nanophotonics* **2017**, *6*, 1289-1308.
- (50). Duong, D. L.; Yun, S. J.; Lee, Y. H., van der Waals Layered Materials: Opportunities and Challenges. *ACS Nano* **2017**, *11*, 11803-11830.

- (51). Xiao, D.; Liu, G.-B.; Feng, W., *et al.*, Coupled Spin and Valley Physics in Monolayers of MoS₂ and Other Group-VI Dichalcogenides. *Phys Rev Lett* **2012**, *108*, 196802.
- (52). Zhou, Y.; Scuri, G.; Wild, D. S., *et al.*, Probing dark excitons in atomically thin semiconductors via near-field coupling to surface plasmon polaritons. *Nat Nanotechnol* **2017**, *12*, 856-860.
- (53). Molas, M. R.; Faugeras, C.; Slobodeniuk, A. O., *et al.*, Brightening of dark excitons in monolayers of semiconducting transition metal dichalcogenides. *2D Mater* **2017**, *4*, 021003.
- (54). Zhang, X. X.; Cao, T.; Lu, Z., *et al.*, Magnetic brightening and control of dark excitons in monolayer WSe₂. *Nat Nanotechnol* **2017**, *12*, 883-888.

Figure captions

Figure-1.

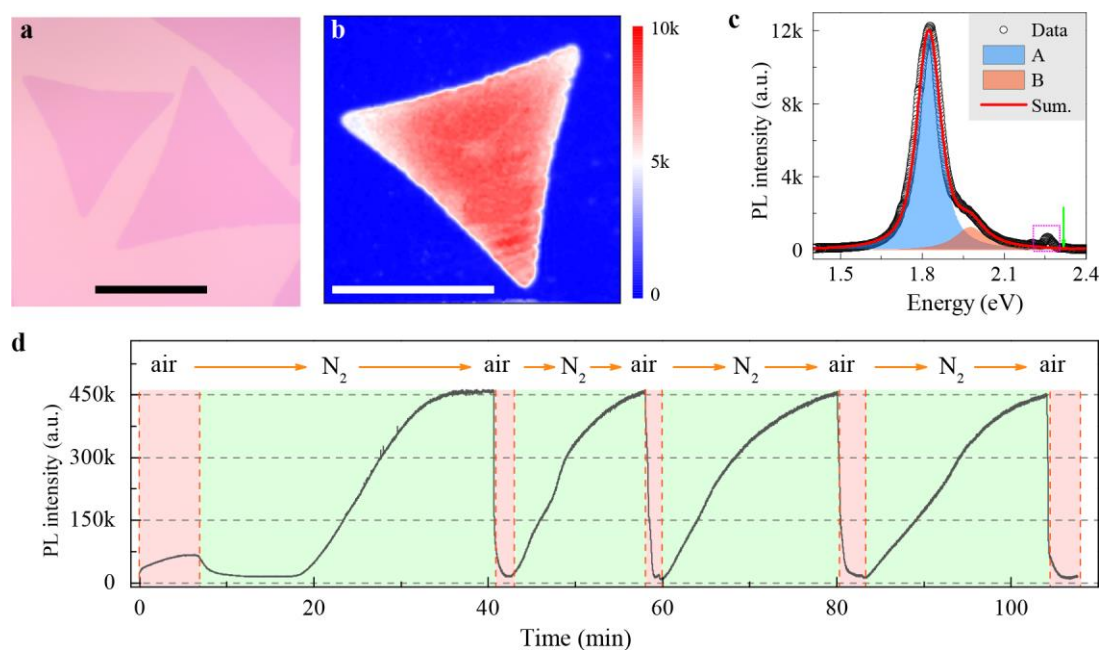


Figure 1. (a) Optical image, (b) photoluminescence (PL) image, and (c) PL spectra of the prepared monolayer MoS₂. Scale bar: 20 μm . The spectral profile was deconvoluted by two Voigt functions. The weak peak highlighted by the dashed box is the Raman signal of monolayer MoS₂. (d) PL trajectory of monolayer MoS₂ under laser irradiation under controlled gas environments. The irradiation and excitation light are both 532 nm CW laser (denoted by the arrow in c). The power density was 21 MW/cm². Red shades indicate PL behaviors in the air atmosphere, and green shades indicate that in N₂ atmosphere. Switching between N₂ and Air is achieved by opening or closing the vacuum valve on the top of the chamber. Dashed lines are provided to guide the eyes.

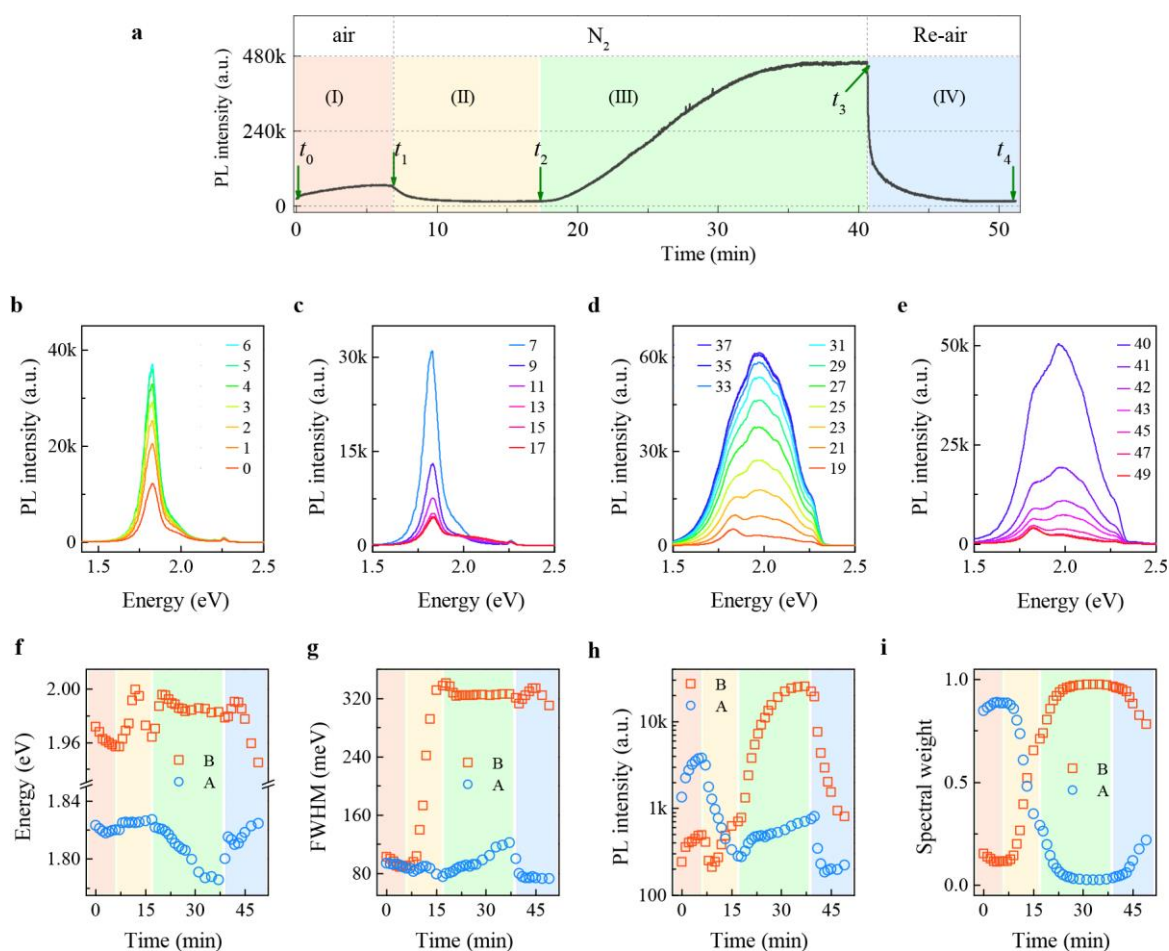
Figure-2

Figure 2. PL evolution of monolayer MoS₂ during laser irradiation. (a) The PL trajectory is divided into four stages. The laser power density was 21 MW/cm² for stage I to III, and 3.5 MW/cm² for stage IV, respectively. For the convenience of comparison, PL intensity of stage IV has been magnified. For stage I (red) and IV (blue), MoS₂ was exposed to the air. For stage II (yellow) and III (green), MoS₂ was in N₂ atmosphere. t_0 to t_4 are marked to illustrate the beginning and/or the end of each stage. Dashed lines are provided to guide the eye for comparing PL intensity. (b)-(e) are the spectral profiles of the four stages. The integration time was 3 s; the interval between each spectrum was 1 minute. (f) Photon energies, (g) full width at half maxima (FWHM), (h) the integrated

PL intensity, and (i) spectral weight of A and B excitons as the function of irradiation times. All the parameters are determined by deconvoluting the spectral profiles via Voigt functions.

Figure-3

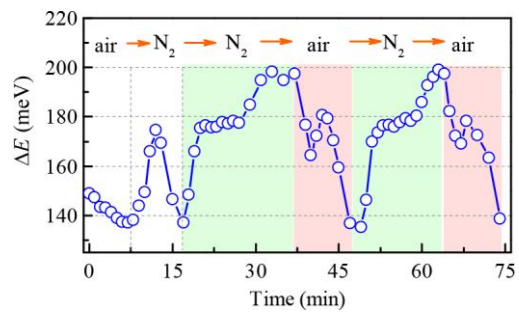


Figure 3. Spin-orbit splitting of monolayer MoS₂ as a function of irradiation time during laser irradiation and switching of gases.

Figure-4

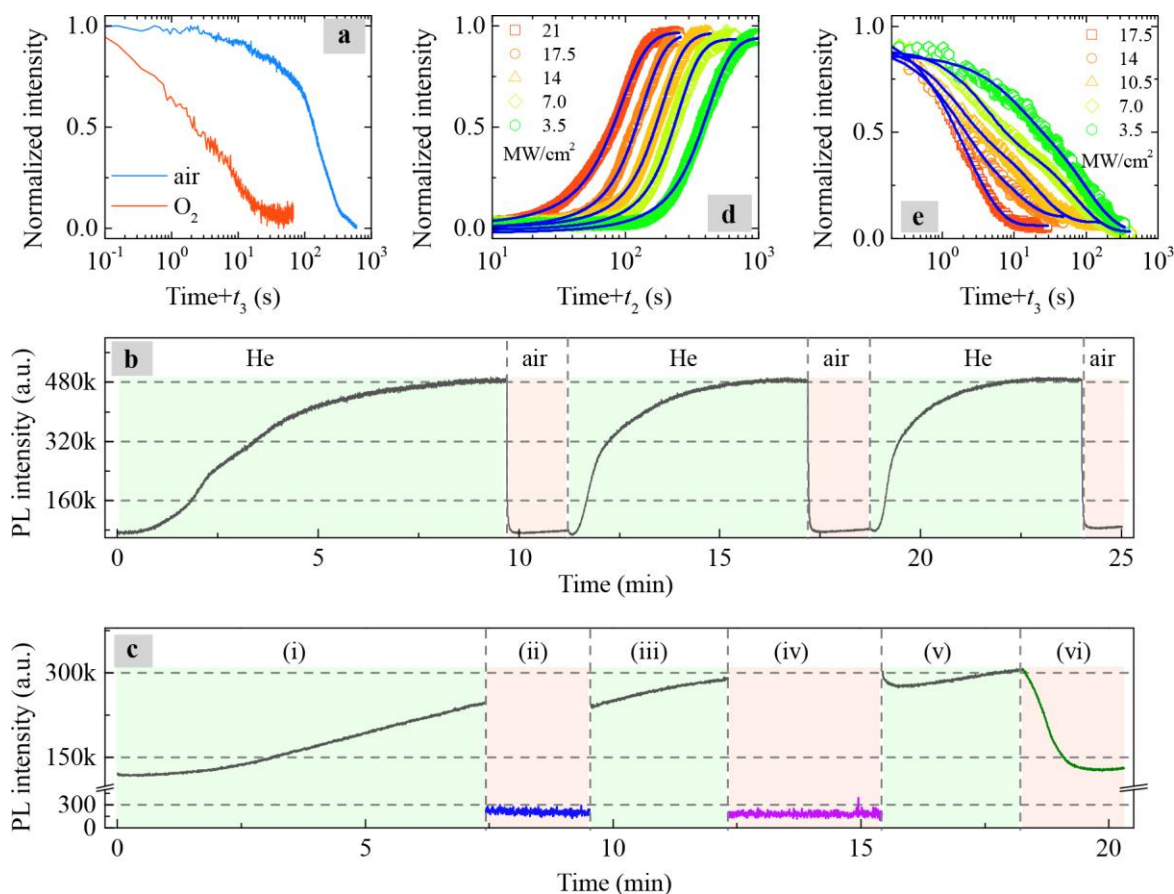


Figure 4. (a) PL evolution under pure oxygen (O₂) and air conditions. The irradiation power density was 3 MW/cm². (b) PL trajectory of monolayer MoS₂ against gases cycling between He and air atmosphere. (c) PL trajectory of monolayer MoS₂ in different conditions. (i, iii, v) Both laser and N₂ are switching on. (ii) Switching off the laser but holding N₂ atmosphere. (iv) Both laser and N₂ are switching off. (vi) Switching off N₂ atmosphere but holding laser excitation. The irradiation power density in b and c was both 21 MW/cm². (d) PL enhancement in N₂ atmosphere, and (e) PL quenching in air atmosphere under laser irradiation with different power densities, respectively. The solid lines in d and e are the fitting results by the corresponding equations discussed in the main context.

Figure-5

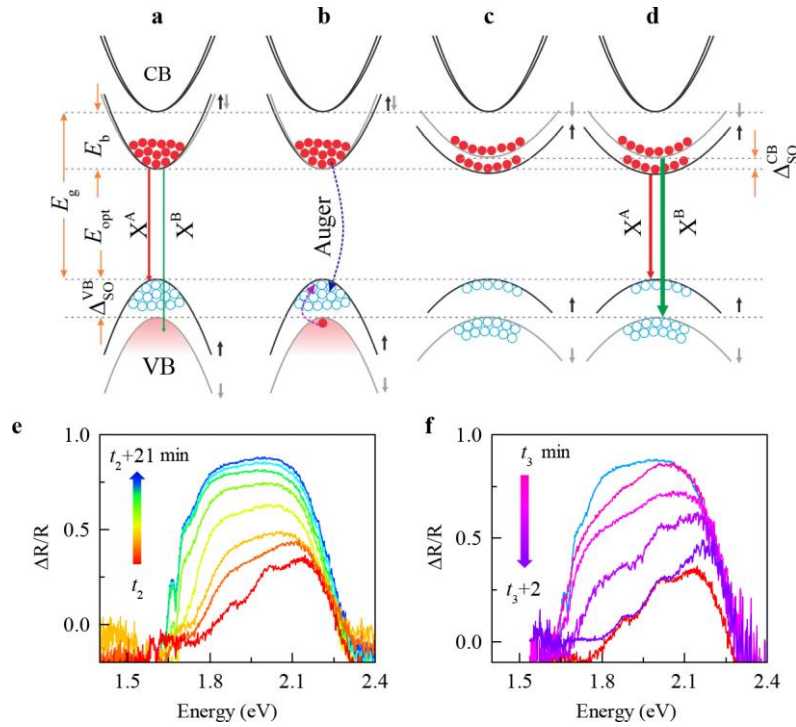


Figure 5. Schematic illustration of spin-orbit coupling engineering in monolayer MoS₂. Filled (red) and empty (blue) circles indicate the electrons and holes. CB (VB) represents the conduction band (valence band). The spin-up (spin-down) subbands are denoted by the arrows in black (gray) colors. E_g , E_{opt} , and E_b represent the electronic bandgap, optical bandgap, and the binding energy of excitons, respectively. Δ_{SO}^{VB} and Δ_{SO}^{CB} indicate the corresponding spin-orbit splitting of VB and CB. (a) Under low carrier concentrations, the radiative recombination of electrons and holes leads to the PL emission of A exciton (X^A). (b) Under high carrier concentrations, Auger recombination becomes dominant, which will annihilate two electrons (one in CB, one in B sub-bands) and a hole (in A sub-band) by the non-radiative process. (c) Auger recombination results in the population of holes in B subband, and subsequent band renormalizations. (d) The radiative recombination of electrons and holes in B sub-band

leads to the PL emission of B exciton. Evolution of reflectance contrast spectra during stage III (e) and stage IV (f) processes shown in Fig. 2. t_2 and t_3 denote the beginning of the two approaches, as marked in Figure 2a. The time intervals for e and f are 3 min and 20 s, respectively. The highest and lowest curves in F are the end and beginning reflectance spectra in stage III (in e).